



**HAL**  
open science

## **A study on wildfire impacts on greenhouse gas emissions and regional air quality in South of Orléans, France**

Chaoyang Xue, Gisèle Krysztofiak, Yangang Ren, Min Cai, Patrick Mercier, Frédéric Le Fur, Corinne Robin, Benoit Grosselin, Véronique Daële, Max McGillen, et al.

### ► To cite this version:

Chaoyang Xue, Gisèle Krysztofiak, Yangang Ren, Min Cai, Patrick Mercier, et al.. A study on wildfire impacts on greenhouse gas emissions and regional air quality in South of Orléans, France. *Journal of Environmental Sciences*, 2024, 135, pp.521-533. 10.1016/j.jes.2022.08.032 . hal-03903263

**HAL Id: hal-03903263**

**<https://hal.science/hal-03903263>**

Submitted on 16 Dec 2022

**HAL** is a multi-disciplinary open access archive for the deposit and dissemination of scientific research documents, whether they are published or not. The documents may come from teaching and research institutions in France or abroad, or from public or private research centers.

L'archive ouverte pluridisciplinaire **HAL**, est destinée au dépôt et à la diffusion de documents scientifiques de niveau recherche, publiés ou non, émanant des établissements d'enseignement et de recherche français ou étrangers, des laboratoires publics ou privés.

1 **A Study on Wildfire Impacts on Greenhouse Gas Emissions and Regional Air**  
2 **Quality in South of Orléans, France**

3 Chaoyang Xue<sup>1</sup>, Gisèle Krysztofiak<sup>1</sup>, Yangang Ren<sup>2, 3</sup>, Min Cai<sup>2</sup>, Patrick Mercier<sup>4</sup>, Frédéric Le  
4 Fur<sup>4</sup>, Corinne Robin<sup>4</sup>, Benoit Grosselin<sup>2</sup>, Véronique Daële<sup>2</sup>, Max R. McGillen<sup>2</sup>, Yujing Mu<sup>3</sup>,  
5 Valéry Catoire<sup>1, \*</sup>, Abdelwahid Mellouki<sup>2, 5, \*</sup>

6  
7 <sup>1</sup> Laboratoire de Physique et Chimie de l'Environnement et de l'Espace (LPC2E), CNRS –  
8 Université Orléans – CNES (UMR 7328), 45071 Orléans Cedex 2, France

9 <sup>2</sup> Institut de Combustion, Aérothermique, Réactivité Environnement (ICARE), CNRS, 45071  
10 Orléans Cedex 2, France

11 <sup>3</sup> Research Centre for Eco-Environmental Sciences, Chinese Academy of Sciences, Beijing  
12 100085, China

13 <sup>4</sup> Lig'Air- Association de surveillance de la qualité de l'air en région Centre-Val de Loire, 45590  
14 Saint-Cyr-en-Val, France

15 <sup>5</sup> Mohammed V University, Rabat, Morocco

16  
17 Correspondence:

18 Abdelwahid Mellouki ([mellouki@cnrs-orleans.fr](mailto:mellouki@cnrs-orleans.fr))

19 Valéry Catoire ([valery.catoire@cnrs-orleans.fr](mailto:valery.catoire@cnrs-orleans.fr))

## 20 Abstract

21 Wildfire events are increasing globally which may be partly associated with climate change,  
22 resulting in significant adverse impacts on local, regional air quality and global climate. In  
23 September 2020, a small wildfire (burned area: 36.3 ha) event occurred in Souesmes (Loir-et-  
24 Cher, Sologne, France), and its plume spread out over 200 km on the following day as observed  
25 by the MODIS satellite. Based on measurements at a suburban site (~50 km northwest of the fire  
26 location) in Orléans and backward trajectory analysis, young wildfire plumes were characterized.  
27 Significant increases in gaseous pollutants (CO, CH<sub>4</sub>, N<sub>2</sub>O, VOCs, etc.) and particles were found  
28 within the wildfire plumes, leading to a reduced air quality. Emission factors of various trace  
29 gases and black carbon were determined accordingly and compared with previous studies.  
30 Changes in the ambient ions (such as ammonium, sulfate, nitrate, chloride, and nitrite in the  
31 particle- and gas- phase) and aerosol properties (e.g., aerosol water content, aerosol pH) were  
32 also quantified and discussed. Moreover, we estimated the total carbon and climate-related  
33 species (e.g., CO<sub>2</sub>, CH<sub>4</sub>, N<sub>2</sub>O, and BC) emissions and compared them with fire emission  
34 inventories. Current biomass burning emission inventories have uncertainties in estimating small  
35 fire burned areas and emissions. For instance, we found that the Global Fire Assimilation System  
36 (GFAS) may underestimate emissions (e.g., CO) of this small wildfire while other inventories  
37 (GFED and FINN) showed significant overestimation. Considering that it is the first time to  
38 record wildfire plumes in this region, related atmospheric implications are presented and  
39 discussed.

## 40 Keywords

41 Wildfire; Air Quality; Emission Factor; Emission Inventory; VOLTAIRE Supersite.

## 42 Highlights

- 43 1. Young wildfire plumes were observed and documented for the first time in suburban Orléans  
44 city, France.
- 45 2. Regional air quality was reduced by the wildfire emissions.
- 46 3. Emission factors of various pollutants were derived and compared with the literature.

47 4. Current biomass burning emission inventories have uncertainties in estimating small fire  
48 emissions.

## 49 1 Introduction

50 The frequency of wildfire events as well as the extent of the burned areas shows an increasing  
51 trend globally due to climate change (Artés et al., 2019; Barbero et al., 2015; Liu et al., 2010;  
52 Randerson et al., 2012). During the combustion of biomass, numerous pollutants, including  
53 particles and gases, are emitted into the atmosphere, which could have potential impacts on air  
54 quality and global climate (Andreae, 2019; Jaffe and Wigder, 2012; Jost et al., 2003; Randerson  
55 et al., 2012).

56 On a regional scale, the emitted pollutants could exacerbate air pollution downwind of the  
57 wildfire. For instance, David et al. (2021) found that wildfire events in the US significantly  
58 enhanced the nationwide particulate matter with aerodynamic diameters smaller than 2.5 or 10  
59  $\mu\text{m}$  ( $\text{PM}_{2.5}$  and  $\text{PM}_{10}$ ). Considering that the number and severity of wildfire events are  
60 increasing, they suggested that wildfire impacts should be considered in the national ambient air  
61 quality standards and implementations. Besides, the emitted pollutants also affect ground-level  
62  $\text{O}_3$  (Jaffe and Wigder, 2012). As a secondary pollutant,  $\text{O}_3$  could be consumed or accumulated  
63 within a biomass burning (wildfire) plume varying from different aging stages. In a very fresh  
64 plume,  $\text{O}_3$  is typically consumed regarding its rapid reaction with the emitted NO. It is also  
65 possible that in the very early stages of plume formation, highly reactive organic molecules may  
66 serve to suppress ozone concentrations. As the plume is diluted and transported,  $\text{O}_3$  can be  
67 produced through chemical reactions involving volatile organic compounds (VOCs) and  $\text{NO}_x$   
68 ( $\text{NO} + \text{NO}_2$ ) under sunlight irradiation (Granier et al., 2000; Jaffe and Wigder, 2012). For  
69 example, Wang et al. (2021) observed 10-40 ppbv  $\text{O}_3$  enhancement at 30 km downwind of a  
70 wildfire in the US. In addition, when the plumes (typically VOC-rich) mix into urban plumes  
71 (typically  $\text{NO}_x$ -rich) substantial enhancement in  $\text{O}_3$  formation is observed, which deteriorates  
72 urban air quality (Xu et al., 2021).

73 Carbon monoxide (CO) is considered to be the second-largest primary carbon compound (after  
74 carbon dioxide,  $\text{CO}_2$ ) emitted from the wildfire processes, which accounts for nearly half of its  
75 global emissions (Zheng et al., 2019). CO is typically treated as a tracer for incomplete  
76 combustion, including biomass burning. The tropospheric lifetime of CO against OH with a

77 global mean of  $1.5 \times 10^6$  molecules  $\text{cm}^{-3}$  (Seinfeld and Pandis, 2016) is about 5 weeks, implying  
78 that its concentration in the wildfire plume is dominated by the downwind dilution during  
79 transport over one week or so. Hence, the Emission factor ( $\text{EF}(X) = \Delta X / \Delta \text{CO}$ , where X represents  
80 the target species) of  $\text{O}_3$  obtained in the wildfire plume was usually used for estimating the  
81 plume age (Jaffe and Wigder, 2012). Generally, its values were reported to be negative in a fresh  
82 wildfire plume and turned positive and increased progressively with the plume age (Jaffe and  
83 Wigder, 2012).

84 In addition to the long-lived greenhouse gases (GHGs, e.g.,  $\text{CO}_2$ ,  $\text{CH}_4$ ,  $\text{N}_2\text{O}$ ), non-methane  
85 hydrocarbons (NMHCs) could also be emitted from wildfires. Due to their high reactivity (with  
86  $\text{OH}$ ,  $\text{O}_3$ , or  $\text{NO}_3$ ), NMHCs play important role in the in-plume photochemistry to produce  
87 secondary pollutants like particulate matter (PM),  $\text{O}_3$ , and other photo-oxidants. Furthermore,  
88 numerous NMHCs are toxic and the increase in their ambient concentration levels constitutes a  
89 risk to public health. To quantify their emissions from wildfires, their emission factors can be  
90 calculated (Andreae, 2019; Jost et al., 2003).

91 On a global scale, wildfires are an important GHG source (Friedlingstein et al., 2020; Saunio et  
92 al., 2020). Saunio et al. (2020) have estimated  $17 \text{ Tg CH}_4 \text{ yr}^{-1}$  emissions from wildfire  
93 emissions from 2008 to 2017, which represents 5% of the total anthropogenic  $\text{CH}_4$  emissions. In  
94 addition to GHGs emissions, depending on their size and location, wildfire plumes can be  
95 transported to the upper troposphere-lower stratosphere (UTLS) region, and hence, impact the  
96 global climate and stratospheric ozone layer (Baray et al., 2012; Hirsch and Koren, 2021;  
97 Hooghiem et al., 2020; Kloss et al., 2021, 2019; Yu et al., 2019). For example, Hirsch and Koren  
98 (2021) reported a record-breaking aerosol level in the stratosphere over the southern hemisphere  
99 caused by the intensive Australian bushfires. This wildfire smoke could have a lifetime of days  
100 to months, which allows the smoke to be uniformly mixed over most of the southern hemisphere,  
101 leading to a significant cooling effect of  $1.0 \pm 0.6 \text{ W m}^{-2}$ .

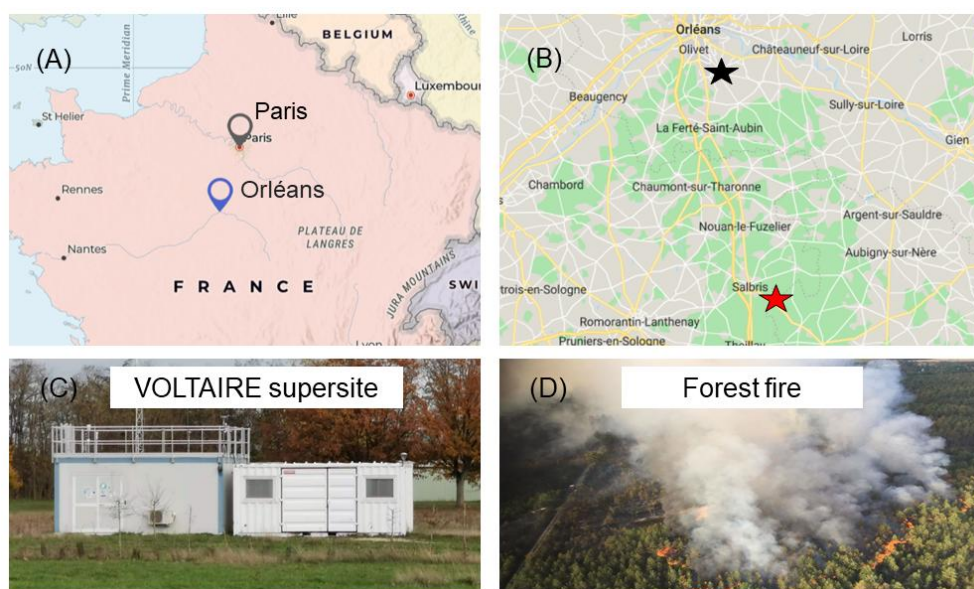
102 Satellite observations can be used for estimating the burned area and emissions of wildfires.  
103 However, scaling this to small fires remains challenging (Ramo et al., 2021; Saunio et al.,  
104 2020). For instance, Ramo et al. (2021) found that the Moderate Resolution Imaging  
105 Spectroradiometer (MODIS) images underestimated the burned area of small fires ( $<100 \text{ ha}$ ) by  
106 94% in sub-Saharan Africa. Hence, the regional impact on air quality and/or the global impact on  
107 climate from both small and large fires should be studied (Ramo et al., 2021), in particular in

108 those regions where few fire events were recorded. Herein, in the middle of September 2020, a  
109 wildfire occurred in southern Orléans city where few wildfire events have occurred in the past.  
110 To the best of our knowledge, no study has been conducted to quantify the impacts of wildfires  
111 on the air quality in this region. Based on atmospheric measurements along with trajectory model  
112 simulations, the impact of this wildfire on the air quality in suburban Orléans was quantified.  
113 Emissions of this wildfire were evaluated and compared with the fire emission inventories.  
114 Atmospheric implications are presented after analysis and discussion of the field measurements  
115 and model simulations.

## 116 2 Methods

### 117 2.1 The Sologne Forest Fire Event

118 At 15:44 (local time, UTC+2) on 14<sup>th</sup> September 2020, firemen in Orléans received the  
119 information about the fire in the Sologne forest (47.3726°N, 2.12987° E, Figure 1). Its spread  
120 was controlled but it was still active at 2:31 on 15<sup>th</sup> September (information obtained from  
121 Firefighters Loire-et-Cher, <https://sdis41.fr/>, last access: 17 January 2022). On 22<sup>nd</sup> September,  
122 the fire was considered permanently extinguished. In total, about 36.3 hectares of forests  
123 (vegetation above ground: coniferous trees, mainly Laricio pines; surface vegetation: heather,  
124 moors, etc.) were burned during this event.



125  
126 Figure 1. (A): Locations of Paris and Orléans (obtained from <https://www.arcgis.com/>, last  
127 access: 25 February 2022); (B): Locations of the forest fire (red star) and the VOLTAIRE

128 supersite (black star). Map base: © Google Map. (C) Photo of the VOLTAIRE supersite (©  
129 Chaoyang Xue); (D): Photo of the fire (© SDIS41).

## 130 2.2 Measurement Site and Instrumentation

131 Measurements used in this study were conducted at the VOLTAIRE supersite. It is located on the  
132 campus of the Centre National de Recherche Scientifique (CNRS, 47.8377° N, 1.9445° E) which  
133 is about 10 km south from Orléans city center and about 120 km southwest from Paris (Figure 1).  
134 Details about this station can be found in previous studies based on measurements at this site  
135 (Cai et al., 2022; Jiang et al., 2017).

136 At this site, NO<sub>x</sub> (NO + NO<sub>2</sub>), O<sub>3</sub>, and meteorological parameters (temperature, pressure, relative  
137 humidity, solar radiation, wind speed, and wind direction) are continuously measured by a  
138 chemiluminescence technique (Model 42i, Thermo Fisher Scientific), a UV photometric analyzer  
139 (Model 49i, Thermo Fisher Scientific), and an auto meteorological station (Model CR800,  
140 Campbell Scientific), respectively. VOCs were measured online by a gas chromatographic (GC)  
141 system (airmoSCAN XPERT, Chromatotec®), with two different separation columns and three  
142 detectors (two flame ionization detectors and one quadrupole mass spectrometer). CO, NO<sub>2</sub>,  
143 CH<sub>4</sub>, and N<sub>2</sub>O were measured by a three-channel infrared absorption spectrometer with quantum  
144 cascade lasers named SPIRIT, with a time resolution of 1.6 s (Brocchi et al., 2019; Catoire et al.,  
145 2017; Kryzstofiak et al., 2018). Particulate matter was measured by an aerosol spectrometer  
146 Fidas<sup>®</sup> 200 (Palas®, Germany), analyzing ambient air in the size range of 180 nm – 18 μm  
147 (recording on PM<sub>1</sub>, PM<sub>2.5</sub>, PM<sub>4</sub>, and PM<sub>10</sub>). A URG-9000D Ambient Ion Monitor (AIM) was  
148 operated to measure gaseous pollutants (acetate, formate, NH<sub>3</sub>, HONO, etc.) and PM<sub>10</sub>  
149 composition (Cl<sup>-</sup>, NO<sub>3</sub><sup>-</sup>, SO<sub>4</sub><sup>2-</sup>, NH<sub>4</sub><sup>+</sup>, Na<sup>+</sup>, K<sup>+</sup>, etc.). Black carbon (BC) was measured by a black  
150 carbon monitor (Magee Scientific Aethalometer<sup>®</sup> Model AE33), which also includes the  
151 aethalometer model to quantify the contributions of wood-burning (BC<sub>w</sub>d) and fossil fuel (BC<sub>ff</sub>)  
152 (Herich et al., 2011).

## 153 2.3 Models

154 The Lagrangian transport and diffusion model, FLEXible PARTicle (FLEXPART) v10.4, was  
155 used to calculate back trajectories of air masses reaching our measurement site (Brocchi et al.,  
156 2018; Pisso et al., 2019). The model simulation was based on ERA5 reanalysis data (grid  
157 resolution: 0.25°×0.25°, <https://www.ecmwf.int/en/forecasts/datasets/reanalysis-datasets/era5>,

158 last access: 17 January 2022) from European Center for Medium-range Weather Forecasts  
159 (ECMWF, <https://www.ecmwf.int/>, last access: 17 January 2022) was used for FLEXPART  
160 simulations (Hersbach et al., 2020). To obtain the trajectory frequency in the whole of September  
161 2020, the HYbrid Single-Particle Lagrangian Integrated Trajectory Model (HYSPLIT,  
162 <https://www.ready.noaa.gov/HYSPLIT.php>, last access: 17 January 2022) was used.  
163 To estimate the aerosol pH, an aerosol thermodynamic model, ISORROPIA II,  
164 ([http://nenes.eas.gatech.edu/ISORROPIA/index\\_old.html](http://nenes.eas.gatech.edu/ISORROPIA/index_old.html), last access: 17 January 2022), was  
165 used (Fountoukis and Nenes, 2007). The model was run based on the AIM data (particle- and  
166 gas-phase), temperature, and relative humidity.

## 167 2.4 Inventories

168 Data from three fire emission inventories were used in this study. The Global Fire Assimilation  
169 System (GFAS, <https://www.ecmwf.int/en/forecasts/dataset/global-fire-assimilation-system>, last  
170 access: 17 January 2022) can provide daily emissions with a spatial resolution of  $0.1^\circ \times 0.1^\circ$  (Di  
171 Giuseppe et al., 2018). The FINN inventory (Fire INventory from NCAR) was developed by  
172 Wiedinmyer et al. (2011), and the data is available at  
173 <https://www2.acom.ucar.edu/modeling/finn-fire-inventory-ncar> (last access: 17 January 2022).  
174 Here we used a file configuration of FINNv2.4 with fire count of MODIS+VIIRS or MODIS,  
175 year of 2020, and speciation of GEOS-Chem. Daily emissions with a horizontal resolution of  
176 1km are provided by this inventory. The GFED inventory (Global Fire Emissions Database,  
177 GFED4.1s, <https://www.globalfiredata.org/>, last access: 17 January 2022) developed by Van Der  
178 Werf et al. (2017) was also used in this study. It has a spatial resolution of  $0.25^\circ \times 0.25^\circ$ . Monthly  
179 emissions with daily fractions are provided in this inventory. In addition, both GFAS and GFED  
180 inventories use emission factors from Andreae and Merlet (2001) and its corresponding update  
181 (Andreae, 2019) while the FINN inventory uses emission factors from Akagi et al. (2011).

## 182 3 Results and Discussion

### 183 3.1 General Overview of the Measurements

184 All the observations in the whole of September 2020 are presented and overviewed here to  
185 represent the typical meteorological and air quality conditions, while detailed analysis was

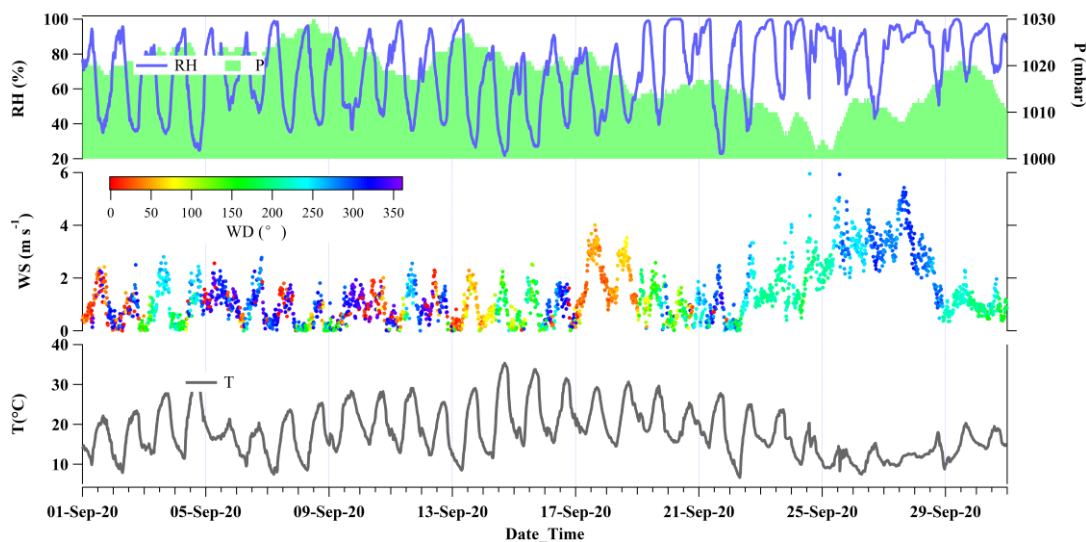


186 mostly focused on the wildfire plume and its comparison with measurements at the same hours  
187 on other days of September.

### 188 3.1.1 Meteorological Conditions

189 During the measurement period, it was mostly sunny and cloud-free except for a limited number  
190 of days (5<sup>th</sup> – 6<sup>th</sup> Sept. and 28<sup>th</sup> Sept. – 1<sup>st</sup> Oct.) when it was rainy or cloudy as reflected by the  
191 measured photosynthetically active radiation (PAR, Figure 2). The air temperature was typically  
192 around 20 °C except for the last week (25<sup>th</sup> Sept. – 1<sup>st</sup> Oct.) when the temperature decreased to  
193 around 10 °C caused by a cold front. The campaign-averaged temperature is  $18.0 \pm 6.0$  °C,  
194 respectively (Table 1). Throughout the campaign, air masses observed at this site originated from  
195 various directions (but few from South/Southeast/East), as reflected by the wind rose plot (Figure  
196 S1A) and the trajectory frequencies obtained from the HYSPLIT model (Figure S1B). Wind  
197 speed was generally less than  $2 \text{ m s}^{-1}$  except for the periods of 17<sup>th</sup> and from 23<sup>rd</sup> to 28<sup>th</sup> Sept.  
198 when the wind speed reached  $4 \text{ m s}^{-1}$ . The average wind speed was  $1.3 \pm 1.0 \text{ m s}^{-1}$  during the  
199 campaign.

200 In particular, the highest temperature of 35.4 °C and the lowest RH of 21.8% during the  
201 campaign occurred at 16:45 on 14<sup>th</sup> September, which is close to the occurrence of the forest  
202 wildfire. Daily average T of  $22.6 \pm 8.8$  °C and RH of  $53 \pm 22\%$  on this day were the highest and  
203 lowest ones during the campaign, respectively. The wind direction was dominated by the south  
204 (the direction of the forest fire location) on the following day after the occurrence of the forest  
205 wildfire, which blew the emitted pollutants to the north of the fire, including the VOLTAIRE  
206 supersite.



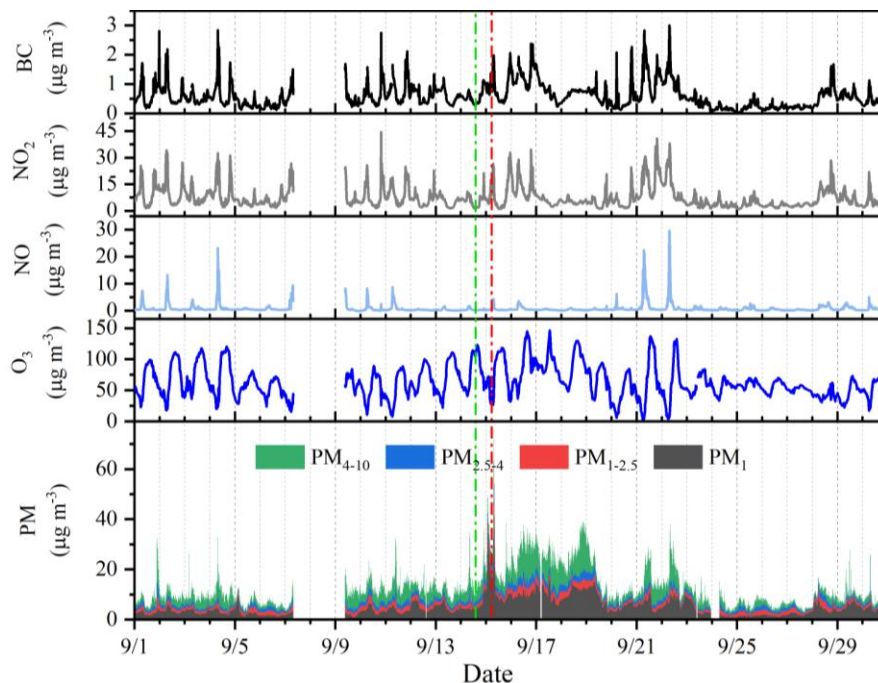
207

208 Figure 2: Meteorological parameters measured at the VOLTAIRE supersite. RH: relative  
209 humidity; P: pressure; WS: wind speed; WD: wind direction; T: temperature.

### 210 3.1.2 Pollutants

211 The VOLTAIRE supersite is located in a relatively clean area with the average  $PM_{2.5}$  ( $6.7 \mu g m^{-3}$ )  
212  $^3$ ),  $PM_{10}$  ( $12.8 \mu g m^{-3}$ ),  $NO_2$  ( $7.4 \mu g m^{-3}$ ), and  $O_3$  ( $63.6 \mu g m^{-3}$ ) being lower than the World  
213 Health Organization (WHO) air quality guideline values (see WHO website:  
214 [https://www.who.int/news-room/fact-sheets/detail/ambient-\(outdoor\)-air-quality-and-health](https://www.who.int/news-room/fact-sheets/detail/ambient-(outdoor)-air-quality-and-health), last  
215 access: 7 March 2022) of  $15 \mu g m^{-3}$  (24 h mean) for  $PM_{2.5}$ ,  $45 \mu g m^{-3}$  (24 h mean) for  $PM_{10}$ ,  $25$   
216  $\mu g m^{-3}$  (24 h mean) for  $NO_2$ , and  $100 \mu g m^{-3}$  (8 h daily maximum) for  $O_3$ . All the pollutants  
217 exhibited much lower values during the period from 23<sup>rd</sup> to 28<sup>th</sup> Sept., as a result of fast dilution  
218 caused by high wind speeds (Figure 2).

219 Regarding the mass distribution of different particle sizes, average concentrations of  $PM_1$ ,  $PM_{1-}$   
220  $2.5$ ,  $PM_{2.5-4}$ , and  $PM_{4-10}$  were  $5.0 \pm 3.9$ ,  $1.7 \pm 0.8$ ,  $1.6 \pm 0.8$ , and  $4.5 \pm 3.7 \mu g m^{-3}$  (Table 1), with  
221 their contributions of 39%, 13%, 13%, and 35% to  $PM_{10}$ , respectively. BC was generally lower  
222 than  $2 \mu g m^{-3}$ , with an average of  $0.6 \pm 0.4 \mu g m^{-3}$ . Significant enhancements in PM and BC were  
223 found in the wildfire plume observed on the morning of 15<sup>th</sup> Sept. and more analysis is presented  
224 in Section 3.2.



225

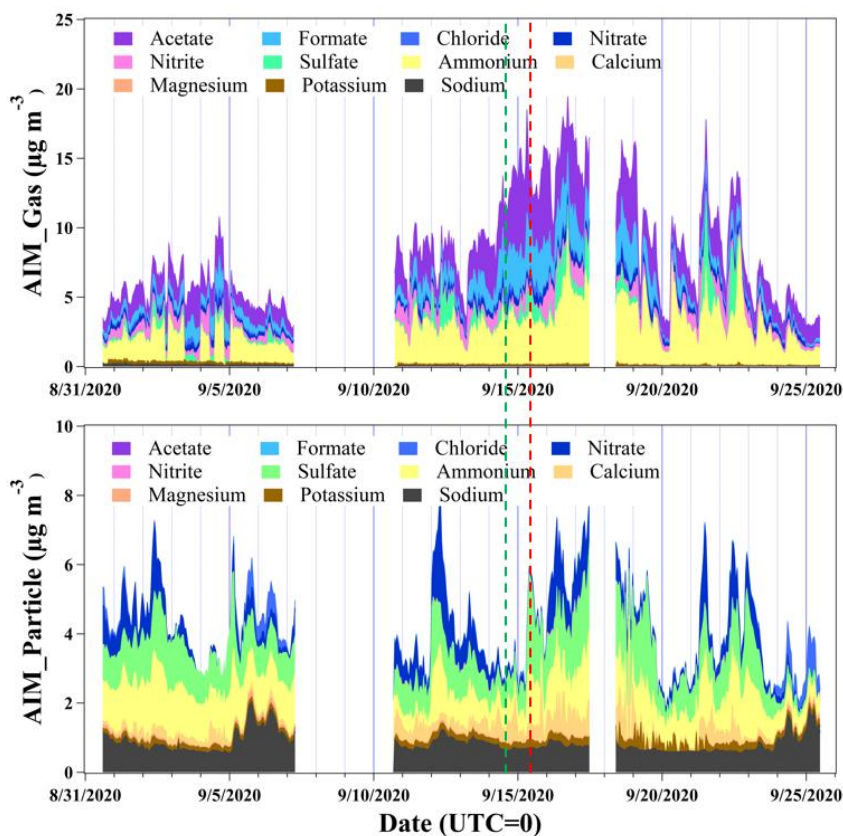
226 Figure 3: Time series of pollutants (PM, O<sub>3</sub>, NO, NO<sub>2</sub> and BC, in µg m<sup>-3</sup>) concentrations at the  
 227 VOLTAIRE supersite (data from Lig'Air, <https://www.ligair.fr/>, last access: 7 March 2022). The  
 228 green and red vertical lines indicate the occurrence of the forest fire in Souesmes and the  
 229 observation of the wildfire plume at the VOLTAIRE supersite.

230 Table 1: Statistic description of the observations at the VOLTAIRE supersite during the whole of  
 231 September 2020. Except for the meteorological parameters, all the pollutants listed in this table  
 232 are in µg m<sup>-3</sup>. For AIM data, p and g represent particle- or gas- phases, respectively.

Parameters	Average	Range	Parameters	Average	Range
T (°C)	18.0±6.0	6.6-35.4	Sulfate (p)	1.1±0.5	≤2.9
PAR (µmol m <sup>-2</sup> s <sup>-1</sup> )	17.7±24.2	0-91.2	Ammonium (p)	1.0±0.4	0.3-2.2
WS (m s <sup>-1</sup> )	1.3±1.0	0-5.9	Calcium (p)	0.3 ± 0.3	≤2.6
RH (%)	70.6±21.0	21.8-100	Magnesium (p)	0.04±0.03	≤0.19
P (mBar)	1018±5.9	1001-1030	Potassium (p)	0.2±0.1	≤0.8
BC	0.6±0.4	≤3.0	Sodium (p)	0.8±0.3	0.6-2.1
NO	0.8±1.9	≤29.7	Acetate (g)	2.4±1.3	0.7-7.4
NO <sub>2</sub>	7.4±6.1	0.9-44.6	Formate (g)	1.1±0.9	0.1-4.1
O <sub>3</sub>	63.6±26.5	2.4-146.4	Chloride (g)	0.19±0.14	0.05-0.90
PM <sub>1</sub>	5.0±3.9	0.6-42.1	Nitrate (g)	0.4±0.2	≤1.1
PM <sub>1-2.5</sub>	1.7±0.8	0.4-9.0	Nitrite (g)	0.7±0.6	0.1-4.4
PM <sub>2.5-4</sub>	1.6±0.8	0.3-7.8	Sulfate (g)	0.5±0.8	≤4.9
PM <sub>4-10</sub>	4.5±3.7	0.1-22.9	Ammonium (g)	2.7±1.4	0.1-4.4
Acetate (p)	(8.7±2.8)×10 <sup>-4</sup>	≤0.002	Calcium (g)	0.04±0.02	0.01-0.16
Formate (p)	(23±8.4)×10 <sup>-3</sup>	≤0.04	Magnesium (g)	(1.8±1.4)×10 <sup>-3</sup>	≤0.02
Chloride (p)	0.13±0.21	≤1.2	Potassium (g)	0.12±0.07	≤0.36
Nitrate (p)	0.5±0.5	≤3.0	Sodium (g)	0.08±0.06	0.03-0.31
Nitrite (p)	0.02±0.01	≤0.06			

233  
 234 Ambient ions in the particle or gas phase are presented in Figure 4. In terms of the measured  
 235 concentrations, sodium and ammonium were the most important cations in the particle phase,  
 236 while nitrate and sulfate were the most important anions. On average, concentrations of sodium,  
 237 ammonium, nitrate, and sulfate were 0.8±0.3, 1.0±0.4, 0.5±0.5, and 1.1±0.5 µg m<sup>-3</sup> (Table 1),

238 with their mass contributions of 19.9%, 24.8%, 13.0%, and 25.9% to the total particle-phase ions  
 239 (Figure S2), respectively. In contrast, the measured organics (acetate and formate), chloride,  
 240 nitrite, calcium, magnesium, and potassium showed much lower levels, with a sum of their  
 241 contributions of 16.4%. In the gas phase, the dominant ions were ammonium (33.2%), acetate  
 242 (28.6%), formate (13.6%), nitrite (8.6%), and sulfate (6.1%) while contributions of other ions  
 243 were all less than 5% (Figure S2).



244  
 245 Figure 4: Gas- (upper panel) and particle-phase compositions of PM<sub>10</sub> (lower panel) measured at  
 246 the VOLTAIRE supersite. The green and red vertical lines indicate the occurrence of the forest  
 247 fire in Souesmes and the observation of the wildfire plume at the VOLTAIRE supersite,  
 248 respectively.

### 249 3.2 Observations of the wildfire Plume

250 Figure S3 shows the concentrations of CO, NO<sub>2</sub>, CH<sub>4</sub>, and N<sub>2</sub>O measured by SPIRIT at the  
 251 supersite. Stable measurements started at 9:27 on 15<sup>th</sup> September and the first measured CO  
 252 concentration was 837 ppbv, which is much higher than the background level of around 100  
 253 ppbv. Later, the highest CO concentration of 1050 ppbv was observed at 09:38. High

254 concentrations of NO<sub>2</sub> (9.3 ppbv), N<sub>2</sub>O (334 ppbv), and CH<sub>4</sub> (2203 ppbv) were also observed  
255 within 10 mins around the CO peak. Meanwhile, the levels of other measured pollutants (e.g.,  
256 PM, BC, sulfate) showed a simultaneous increase (Figure 3 and Figure 4). For example, the  
257 PM<sub>10</sub> level of 75.9 μg m<sup>-3</sup> was the highest one in September and more than 6 times higher than  
258 the campaign average value of 12.7 μg m<sup>-3</sup>, revealing the significant impact of this forest fire on  
259 the air quality in this region. In addition, a view from the satellite (Figure S4) also observed the  
260 wildfire and the regional spread of its emissions.

### 261 3.2.1 Emission Factors (EF)

262 As the forest fire occurred around 15:35 on 14<sup>th</sup> September and the wildfire plume was observed  
263 at 9:38 (local time, the occurrence of the CO peak) on 15<sup>th</sup> September, the plume age should be  
264 <18 h (from the trajectory a plume age <12 h could be obtained and mostly during night-time).  
265 Besides, a significant O<sub>3</sub> decrease by ca. 13 ppbv was observed in this wildfire plume indicating  
266 the plume did not undergo much photochemistry that could lead to O<sub>3</sub> production. For instance,  
267 Jost et al. (2003) found a significant O<sub>3</sub> enhancement in a wildfire plume after 2 h  
268 photochemistry. Hence, the wildfire plume observed here should be relatively fresh (also see the  
269 trajectory in Section 3.3). However, previous field and laboratory studies have reported the  
270 impact of near-source transformation on the properties of wildfire plumes, which may influence  
271 the EF values (Collier et al., 2016; Hodshire et al., 2019; Li et al., 2021). The derived EF values  
272 are focused on gas species, for which the atmospheric oxidization process may cause major  
273 uncertainties. Hence, we employed a method to constrain the uncertainties, which are generally  
274 caused by the chemical loss mainly through OH oxidization. Take toluene as an example, its  
275 reaction rate with OH is 5.6×10<sup>-12</sup> cm<sup>3</sup> molecule<sup>-1</sup> s<sup>-1</sup> at 298 K (Mellouki et al., 2021). Assuming  
276 a relatively high OH concentration of 5×10<sup>5</sup> molecule cm<sup>-3</sup>, a negligible amount of CO but 11%  
277 of toluene will be lost through OH oxidization in 12 hours, leading to an underestimation by  
278 <11% in EF(toluene). Similarly, other EF uncertainties caused by the OH oxidization process  
279 can be estimated, which is summarized in the updated Table 2. Please note that we used a higher  
280 OH concentration to constrain the upper limit of the uncertainties.

281  
282  
283  
284

285  
 286  
 287  
 288  
 289  
 290  
 291  
 292  
 293

Table 2: Emission factors (EF) inferred from the wildfire plume. Units: ppbv ppbv<sup>-1</sup> for Efs of NO<sub>2</sub>, CH<sub>4</sub>, and N<sub>2</sub>O (measured by SPIRIT); μg m<sup>-3</sup> ppbv<sup>-1</sup> for all the others. BTEX = Benzene + Toluene + Ethylbenzene + m/p/o -Xylenes. Comparisons with temperate forest fire summarized in Andreae (2019) were also shown. Note that the original values in Andreae (2019) are given in gram species per kilogram dry matter burned and they are converted to EFs for comparison. Atmospheric OH rate constants were taken from Mellouki et al. (2021) or Atkinson and Arey (2003).

X	EF (X)	Uncertainty %	R <sup>2</sup>	Andreae (2019)
O <sub>3</sub>	-4.9E-2		0.70	
NO	8.8E-4		0.47	2.5E-2
CH <sub>4</sub>	2.3E-1		0.79	8.2E-2
N <sub>2</sub> O	1.7E-2		0.84	1.4E-3
BC	2.8E-4		0.70	1.2E-2
123-TMB	7.8E-6	51	0.99	
124-TMB	1.7E-5	50	0.80	
135-TMB	2.7E-6	71	0.86	
BTEX	1.2E-4		0.62	2.5E-3
Ethylbenzene	1.6E-5	14	1.00	9.7E-5
Toluene	5.2E-5	11	0.90	7.5E-4
α-Pinene	1.3E-5	68	0.69	
n-Octane	8.7E-5	16	0.88	
n-Propylbenzene	7.5E-6	12	0.67	
p-Ethyltoluene	3.5E-6	22	0.92	
m-Diethylbenzene	6.8E-7		0.45	
m-Ethyltoluene	6.2E-6	33	0.95	
methyl ethyl ketone	2.5E-4	35	0.35	
n-Decane	3.5E-6	21	1.00	

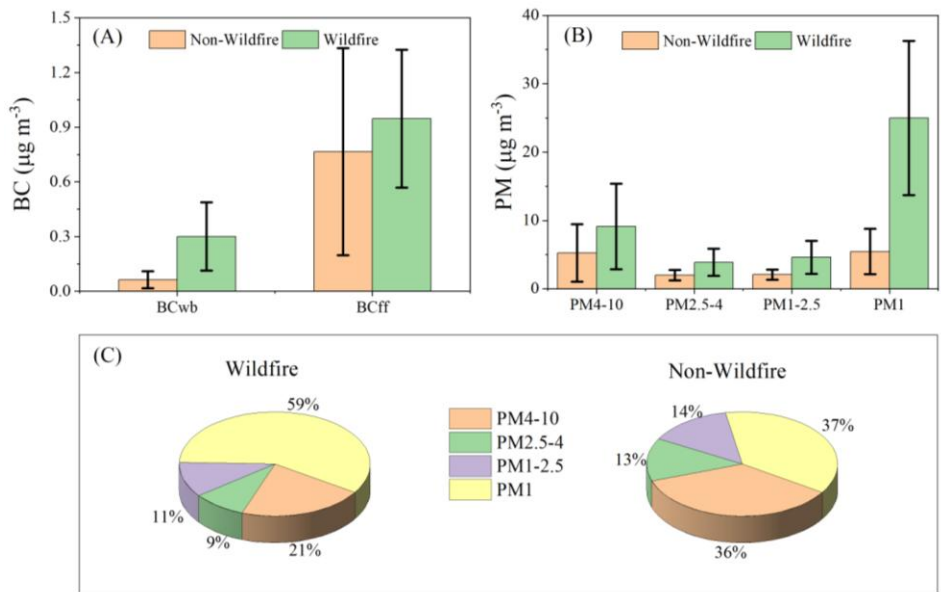
294

295 The molar enhancement ratio of compound X compared to CO was defined as  $EF(X)=\Delta X/\Delta CO$   
296 (Andreae, 2019; Jost et al., 2003), which was used here to estimate the wildfire emissions. To  
297 avoid the uncertainty caused by the selection of background levels, we used the slope of the  
298 regression line between species X and CO as the EF (X) during the pollution case (Jost et al.,  
299 2003). Table 2 shows the derived EFs and the correlations for numerous species. As mentioned  
300 before, a decreased  $O_3$  resulted in a negative  $EF(O_3)$  of  $-0.05 \mu g m^{-3} ppbv^{-1}$  (equivalent to  $-0.026$   
301  $ppbv ppbv^{-1}$ ) was obtained here, indicating a young wildfire plume. Most correlation coefficients  
302 are high, implying that the increase in species X and CO are caused by the same source, the  
303 wildfire plume. Poor correlations between some species (e.g., xylenes, benzene) and CO are also  
304 found, which might be caused by the complexity of the emissions as well as the ambient dilution  
305 process. In particular, significant  $CH_4$  emission reflected by a high  $CH_4$  peak of 2203 ppbv and a  
306 positive  $EF(CH_4)$  of  $0.23 ppbv ppbv^{-1}$  was found in this wildfire plume, implying the burning of  
307 the herbaceous layer (Andreae, 2019; Jost et al., 2003). This may also explain the higher  
308  $EF(CH_4)$  and  $EF(N_2O)$  obtained here than those from the averages of temperate forest fires ( $0.08$   
309 and  $0.001 ppbv ppbv^{-1}$ , respectively) (Andreae, 2019). Other EFs are lower than those from  
310 temperate fires (Andreae, 2019), indicating the potential impact of dilution and highlighting the  
311 complexity of the wildfire emissions and their impacts on ambient pollutant levels. Although this  
312 fire was small (36.3 ha burned area) compared with the fires summarized in Andreae (2019), it  
313 has been suggested that the relatively high EFs for greenhouse gases ( $N_2O$  and  $CH_4$ ) from small  
314 fires may be of importance to the global greenhouse gas budget (Randerson et al., 2012).

### 315 3.2.2 Impacts on BC and Particle Size Distribution

316 We explored the possible impact of this forest fire, even though a small one, on the measured BC  
317 levels and its sources. Figure 5 shows the average concentration of measured  $BC_{wb}$  (BC derived  
318 from wood burning) and  $BC_{ff}$  (BC derived from fossil fuel) in the wildfire plume or non-wildfire  
319 plumes at the same hours (9:00-11:00).  $BC_{ff}$  was the major source for the measured total BC at  
320 this site and about one order of magnitude higher than  $BC_{wd}$  in non-wildfire plumes. Considering  
321 that the measurements covered rush hours, the source of BC in non-wildfire plumes was  
322 attributed to fossil fuel combustion. The corresponding  $BC_{wb}/BC_{ff}$  ratio of 0.08 was in the range  
323 of 0.02 – 0.11 reported in other sites in Europe during summertime (Herich et al., 2011).  
324 However,  $BC_{wd}$  increased significantly in the wildfire plume ( $0.3\pm 0.19 \mu g m^{-3}$ , non-wildfire  
325 plume:  $0.06\pm 0.05 \mu g m^{-3}$ ) while  $BC_{ff}$  kept a similar level ( $0.95\pm 0.38 \mu g m^{-3}$ ) to that in non-

326 wildfire plumes ( $0.77 \pm 0.57 \mu\text{g m}^{-3}$ ), leading to an increasing  $BC_{wb}/BC_{ff}$  ratio of 0.32, which is in  
 327 the range of values (0.3 – 0.5) impacted by wildfire emissions (Helin et al., 2018; Herich et al.,  
 328 2011; Kalogridis et al., 2018; Yttri et al., 2014). This indicates the potential impact of this  
 329 wildfire on regional BC levels.



330  
 331 Figure 5: Levels of (A)  $BC_{wb}$  and  $BC_{ff}$ , and (B) PM at different sizes, and (C) their relative mass  
 332 contributions of different PM sizes to  $PM_{10}$  in the wildfire or non-wildfire plumes during the  
 333 same hours (9:00 – 11:00) considering that the detection of the plume covered rushing hours.

334 Figure 5B and C show PM mass concentrations at different sizes ( $PM_1$ ,  $PM_{1-2.5}$ ,  $PM_{2.5-4}$ , and  
 335  $PM_{4-10}$ ) and their relative contributions in the wildfire or non-wildfire plumes during the same  
 336 hours (9:00 – 11:00). Average  $PM_{2.5}$  (or  $PM_{10}$ ) in the non-wildfire plumes during the same hours  
 337 of the day was 7.5 (or 14.7)  $\mu\text{g m}^{-3}$ , which is much lower than the WHO air quality guideline  
 338  $PM_{2.5}$  (or  $PM_{10}$ ) value of 15 (or 45)  $\mu\text{g m}^{-3}$  (24 h mean). However, in the wildfire plume, the  
 339 average  $PM_{2.5}$  (or  $PM_{10}$ ) increased to 29.6 (or 42.6)  $\mu\text{g m}^{-3}$ , which exceeds (or becomes close to)  
 340 the WHO air quality guideline  $PM_{2.5}$  (or  $PM_{10}$ ) value, indicating a potential public health risk  
 341 caused by wildfire emissions (PM, BC, VOCs, etc.). Moreover, wildfire emissions can cause  
 342 changes in particulate size distribution. For instance, mass concentrations of  $PM_1$ ,  $PM_{1-2.5}$ ,  $PM_{2.5-4}$ ,  
 343 and  $PM_{4-10}$  in the non-wildfire plumes were 5.5, 2.1, 2.0, and 5.2  $\mu\text{g m}^{-3}$ , with relative  
 344 contributions of 37%, 14%, 13%, and 36%, respectively. All their mass concentrations showed a  
 345 significant increase (from 5.5 to 25.0, 2.1 to 4.6, 2.0 to 3.9, and 5.2 to 9.1  $\mu\text{g m}^{-3}$  for  $PM_1$ ,  $PM_{1-2.5}$ ,



346  $_{2.5}$ ,  $PM_{2.5-4}$ , and  $PM_{4-10}$ , respectively), while their contributions changed remarkably within the  
347 biomass burning plume, particularly  $PM_1$  and  $PM_{4-10}$  whose contributions increased to 59% or  
348 decreased to 21%, respectively. As reported in previous studies, wildfire can emit various sizes  
349 of particles. However, particles with a smaller diameter (i.e., submicron particles) hold a  
350 relatively longer atmospheric lifetime against deposition so that they may undergo a regional  
351 transportation process (Gallagher et al., 2002).

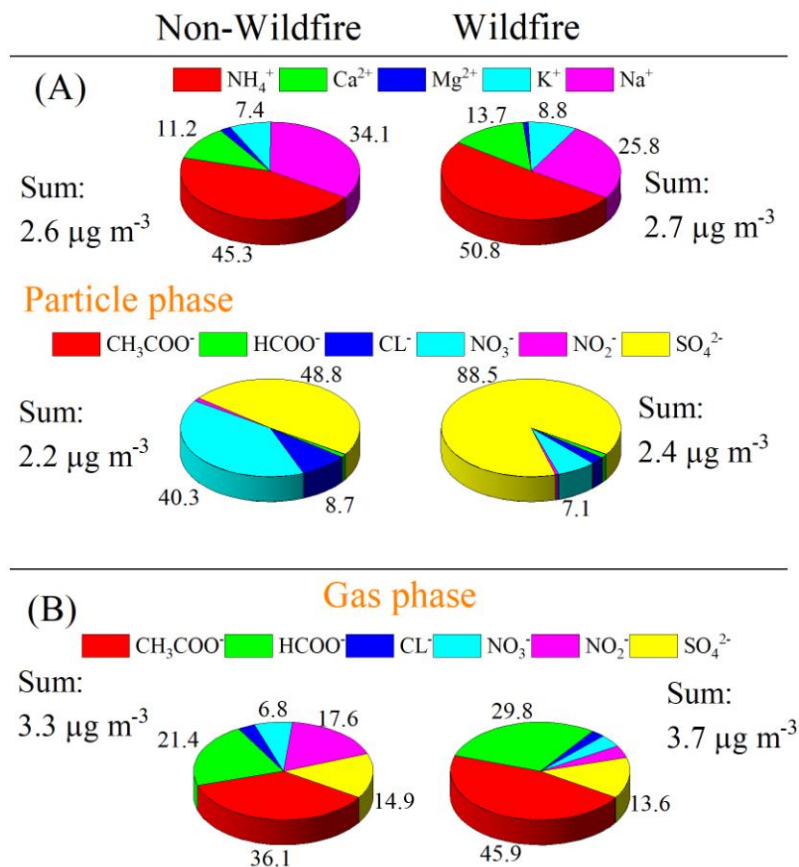
### 352 3.2.3 Impacts on Ambient Ions in the Particle- and Gas-Phase

353 Figure 6A displays the relative mass contribution of each particle-phase cation or anion to their  
354 total masses. During the non-wildfire period, anions were dominated by  $SO_4^{2-}$  and  $NO_3^-$ , with  
355 contributions of 49% and 40%, respectively. Within the young wildfire plume,  $SO_4^{2-}$  was  
356 enhanced from 1.1 to 2.3  $\mu g m^{-3}$  while  $NO_3^-$  reduced from 0.9 to 0.2  $\mu g m^{-3}$ , resulting in a  
357 dominant role of  $SO_4^{2-}$  (89%) in the total particle anion mass.  $NH_4^+$  and  $Na^+$  were the two most  
358 important cations in the particle phase with contributions of 45% and 34% in the non-wildfire  
359 plumes, respectively, which is similar to other European locations (Tang et al., 2021).  $NH_4^+$  was  
360 slightly enhanced from 1.2 to 1.4  $\mu g m^{-3}$  while  $Na^+$  slightly decreased from 0.9 to 0.7  $\mu g m^{-3}$  in  
361 the wildfire plume compared to the non-wildfire plumes, leading to a larger  $NH_4^+$  contribution of  
362 51%.

363 Figure 6B shows the relative mass contribution of each gas-phase cation or anion to their total  
364 masses. The gas-phase anions are typically in their acid forms, i.e., the measured gas-phase  
365  $HCOO^-$ ,  $CH_3COO^-$  and  $NO_2^-$  were in the form of  $HCOOH$ ,  $CH_3COOH$ , and  $HONO$  in the  
366 atmosphere, respectively. A remarkable increase in organic acids ( $CH_3COOH$  and  $HCOOH$ ) was  
367 found within the wildfire plume. Their concentrations increased from 2.0 to 5.7 or from 1.2 to  
368 3.7  $\mu g m^{-3}$ , respectively, suggesting strong emissions of organic acids from the wildfire (Burling  
369 et al., 2010; Chaliyakunnel et al., 2016; R'Honi et al., 2013). Interestingly, significant gas-phase  
370  $SO_4^{2-}$  (i.e.,  $H_2SO_4$ ) enhancement was also found within this wildfire plume as its concentration  
371 increased from 0.8  $\mu g m^{-3}$  to 1.7  $\mu g m^{-3}$ , which may have an impact on sulfate aerosol formation  
372 and new particle formation.

373 No apparent enhancement of  $HONO$  (gas-phase  $NO_2^-$ ) was observed in the wildfire plume,  
374 contrary to previous studies (e.g., Nie et al., 2015; Peng et al., 2020; Theys et al., 2020), which  
375 presented significant  $HONO$  emissions from biomass burning process. Although this does not  
376 preclude the possibility of  $HONO$  emissions from the fire since  $HONO$  concentrations will be

377 affected by dilution and photochemical loss processes (Wang et al., 2021). Gas-phase cation  
 378  $\text{NH}_4^+$  (in the form of  $\text{NH}_3$ ) predominated, with a concentration of 3.1 and  $3.5 \mu\text{g m}^{-3}$  in the non-  
 379 wildfire and wildfire plumes, respectively, which is comparable to other European cities (Tang et  
 380 al., 2021).



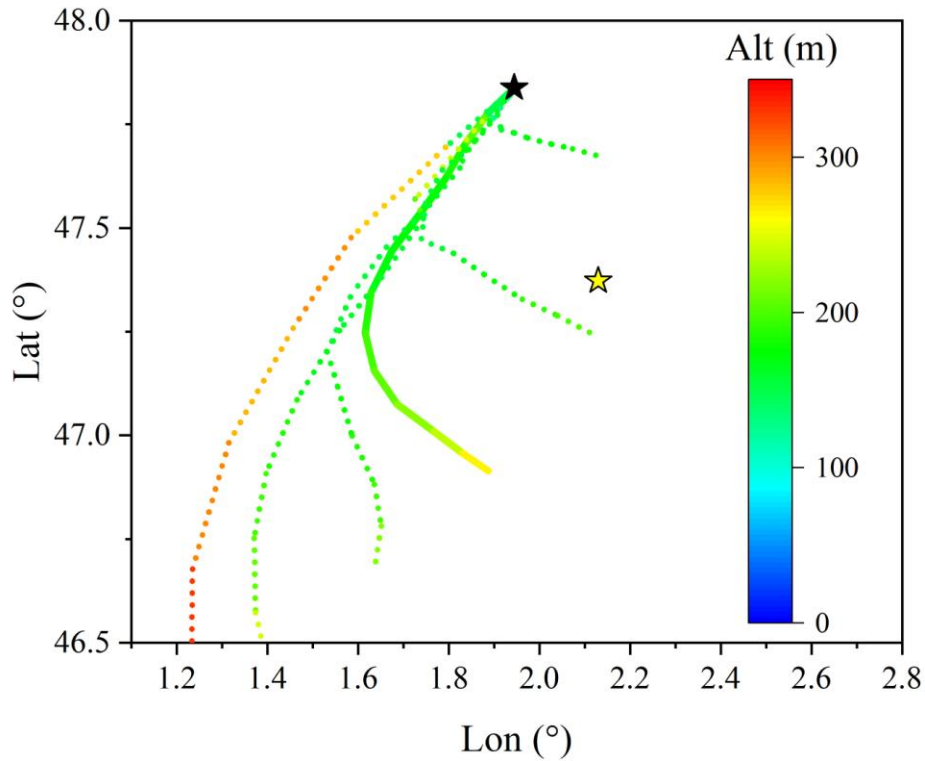
381  
 382 Figure 6: Relative contributions (%) of each cation/anion in the particle-phase (A) and gas-phase  
 383 (B) masses. Percentages less than 5% were not shown. In the gas-phase, concentrations of the  
 384 only cation source,  $\text{NH}_3$ , are  $3.1$  and  $3.5 \mu\text{g m}^{-3}$  during non-wildfire and wildfire periods,  
 385 respectively.

386 3.3 Emission Estimation and Comparison with GFAS

387 3.3.1 FLEXPART Simulations

388 Figure 7 illustrates the 12-h back trajectory (starting from CO peak at 9:38 local time) obtained  
 389 from the FLEXPART simulation. It was found that the air mass at the VOLTAIRE supersite  
 390 mainly originated from the south and southwest, which is consistent with the wind measurements  
 391 at this station on 14<sup>th</sup> and 15<sup>th</sup> September (Figure 2). Some clusters originated from the area

392 above the wildfire (Figure 7). Hence, the large increase in pollutants, such as CO from ~100  
 393 ppbv to 1050 ppbv, is attributed to the transportation of the wildfire plume. The satellite also  
 394 captured the widespread plumes (Figure S4), indicating the impacts of wildfire emissions on  
 395 regional air quality. Besides, quantification of emissions from this wildfire is of significance for  
 396 understanding the role and impacts of small wildfires on regional air quality and global climate.



397  
 398 **Figure 7:** FLEXPART back trajectory with clusters. The black and the yellow stars represent the  
 399 locations of the VOLTAIRE supersite and the wildfire.

400 3.3.2 Emission Estimation vs. GFAS vs. GFED vs. FINN

401 We estimated carbon emissions from this fire event and compared them with current biomass  
 402 burning inventories. A standard equation, developed by Seiler & Crutzen (1980), was popularly  
 403 used for calculating the total carbon emission from a forest fire ( $C_{total}$ ).

404  $C_{total} = A * B * f_c * \beta,$  (Eq-1)

405 where A, B,  $f_c$ , and  $\beta$  represent the total burned area (36.3 ha), biomass density ( $t\ ha^{-1}$ ), the  
 406 fraction of carbon of the biomass, and the fraction of carbon consumed during the burning  
 407 process, respectively. Considering the composition differences, such as organic mat on the forest

408 floor and in peatlands, components on the ground layer and above the ground layer are estimated  
409 separately. French et al. (2002) furtherly modified the equation to:

$$410 \quad C_{total} = A * (B_a * f_{ca} * \beta_a + C_g * \beta_g), \quad (\text{Eq-2})$$

411 where  $B_a$ ,  $f_{ca}$ ,  $\beta_a$ ,  $C_g$ , and  $\beta_g$  denote the average biomass density of the above vegetation ( $\text{t ha}^{-1}$ ),  
412 the carbon fraction of the aboveground biomass with an assumed value of 0.50, the fraction of  
413 the aboveground biomass consumed during the fire, the carbon density ( $15 \text{ t-C ha}^{-1}$  from French  
414 et al. (2002)) of the organic mat exposed to the fire, and the fraction of the organic mat  
415 consumed during the fire, respectively.  $B_a$  was set as  $50 \text{ t ha}^{-1}$  obtained from the European Space  
416 Agency BIOMASS mission (Quegan et al., 2019). 50-year average values of  $\beta_a$  (0.33) and  $\beta_g$   
417 (0.25) for forest fires obtained from French et al. (2002) were adopted in this calculation. Then  
418 we obtained the  $C_{total}$  of  $435.6 \text{ t}$  for this forest fire. This leads to an average carbon emission of  
419  $12 \text{ t-C ha}^{-1}$ , which is comparable to previous studies of  $5 - 40 \text{ t-C ha}^{-1}$  (French et al., 2002;  
420 Randerson et al., 2012).

421 Emission factors of  $\text{CO}_2$ ,  $\text{CO}$ , and  $\text{CH}_4$  during flaming ( $\text{EF}_f$ ,  $\text{kg gas (g total carbon)}^{-1}$ ) and  
422 smoldering ( $\text{EF}_s$ ,  $\text{kg gas (g total carbon)}^{-1}$ ) periods were taken from French et al. (2002) in which  
423 they calculated the average of values reported by several previous studies (Table S1). For  
424 emission factors of  $\text{BC}$  and  $\text{N}_2\text{O}$ , the derived Emission factors in Table 2 were used. As shown in  
425 Table 3, the calculated emissions of  $\text{CO}_2$ ,  $\text{CO}$ ,  $\text{CH}_4$ ,  $\text{BC}$ , and  $\text{N}_2\text{O}$  were 1370 (1128), 82.8 (200),  
426 2.4 (6.6), 0.017 (0.048), and 0.019 (0.054) t (unit: ton), assuming the fire was always at the  
427 flaming (or smoldering) stage, respectively. Note that the actual emission should be between  
428 those two numbers as a wildfire event typically undergoes both flaming and smoldering stages.

429 For the GFAS inventory, emissions were only detected on 14<sup>th</sup> September, with a daily average  
430 of grid CO emission of  $1.5 \times 10^{-9} \text{ kg m}^{-2} \text{ s}^{-1}$ . The total CO emission based on the GFAS inventory  
431 was ca. 11 t. Similarly, the GFAS-derived total carbon,  $\text{CO}_2$ ,  $\text{CH}_4$ ,  $\text{N}_2\text{O}$ , and  $\text{BC}$  emissions from  
432 this wildfire were about 161.4, 1.0, 0.01, 0.05 t, respectively. All the GFAS-derived emissions  
433 except for  $\text{BC}$  and  $\text{N}_2\text{O}$  were much lower than the estimated ones, either  $M_f$  or  $M_s$ .

434 GFED and FINN inventories captured the wildfire on both 14<sup>th</sup> and 15<sup>th</sup>. However, the burned  
435 area in the FINN inventory is largely overestimated, either for fire counted by MODIS (175.5 ha)  
436 or MODIS+VIIRS (270.6 ha). This leads to larger emissions such as total carbon of 2210.7  
437 (1455.6) t,  $\text{CO}_2$  of 7283.8 (4791.0) t,  $\text{CO}$  of 493.3 (328.0) t, etc. in FINN with fire counted by  
438 MODIS+VIIRS (or by MODIS only). Likewise, for the GFED inventory, similar emission levels

439 of total carbon (2553.8 t), CO<sub>2</sub> (8554.2 t), CO (475.2 t), and CH<sub>4</sub> (20.2 t) were obtained.  
 440 However, emissions of BC (2.9 t) and N<sub>2</sub>O (0.77 t) from the GFED inventory are much higher  
 441 than others.

442  
 443  
 444

445 Table 3: Emission factors during flaming (EF<sub>f</sub>, g gas (kg total carbon)<sup>-1</sup>) and smoldering (EF<sub>s</sub>, kg  
 446 gas (g total carbon)<sup>-1</sup>) periods, and the total released mass of each gas/particle during the two  
 447 periods (M<sub>f</sub> and M<sub>s</sub>, in t).

Emissions	Burned Area (ha)	C <sub>total</sub> (ton)	CO <sub>2</sub> (ton)	CO (ton)	CH <sub>4</sub> (ton)	BC (ton)	N <sub>2</sub> O (ton)
Estimation	36.3 <sup>a</sup>	453.6	1128 <sup>s</sup> -3145 <sup>f</sup>	82.8 <sup>f</sup> -200 <sup>s</sup>	2.4 <sup>f</sup> -6.6 <sup>s</sup>	0.017 <sup>f</sup> -0.048 <sup>s</sup>	0.019 <sup>f</sup> -0.054 <sup>s</sup>
GFAS		53.1	161.4	11.0	1.0	0.05	0.011
GFED		2553.8	8554.2	475.2	20.2	2.9	0.77
FINN (MODIS+VIIRS)	270.6	2210.7	7283.8	493.3	17.0	0.035	
FINN (MODIS)	175.5	1455.6	4791.0	328.0	11.1	0.022	
FINN <sup>c</sup>	187.5	1560.9	5135.5	352.9	12.0	0.024	

448 <sup>a</sup>: obtained from Sapeurs-Pompiers Loire-et-Cher; <sup>s</sup>: smoldering period; <sup>f</sup>: flaming period. Note that differences between FINN  
 449 (MODIS) and FINN (MODIS+VIIRS) were possibly caused by the fact that the fire was detected twice on 15<sup>th</sup> Sept. in FINN  
 450 (MODIS+VIIRS), which can be obtained from Table S2; <sup>b</sup>: sum of carbon in the form of CO<sub>2</sub>, CO, CH<sub>4</sub>, and BC; <sup>c</sup>: using the  
 451 average of the twice detection.

452 Previous studies reported underestimation of small fire emissions possibly due to the  
 453 uncertainties in burned area estimation (Ramo et al., 2021; Saunois et al., 2020). In the present  
 454 study, we found a similar underestimation by the GFAS inventory. In contrast, significant  
 455 overestimation in the burned area, and total carbon, CO<sub>2</sub>, CO, and CH<sub>4</sub> emissions were found in  
 456 the GFED and the FINN inventories. Regarding the significant overestimation in the burned  
 457 area, in general, the reason is that current inventories use a coarse spatial resolution, such as  
 458 0.25×0.25 for GFED. For the FINN inventory, the burned area was classified according to land  
 459 cover. For instance, in our case, woody savanna/shrublands, temperate forest, and temperate  
 460 evergreen forest were identified in the FINN inventory, then the burned area can be  
 461 overestimated when summing up all the burned areas. As far as we know, a new version of the  
 462 FINN inventory is forthcoming (<https://www2.acom.ucar.edu/modeling/finn-fire-inventory-ncar>,  
 463 last access: 11 July 2022), which should improve the performance in estimating small fire

464 emissions. Hence, improvement of the inventory performance in small fire emissions is needed  
465 to quantify emissions of small fires and their environmental impacts. Differences between  
466 different inventories also suggest the necessary inter-comparison between inventories.

#### 467 4 Conclusion and Implication

468 In the middle of September 2020, a forest wildfire occurred in the Sologne forest in Souesmes  
469 (Loir-et-Cher, Sologne, France) and its plume spread to 200 km in the following day, as  
470 observed by the MODIS satellite. At the VOLTAIRE supersite in suburban Orléans (about 50  
471 km northwest of the wildfire location), instruments for various trace gases and particle  
472 compositions detected young biomass burning plumes from this wildfire. The data obtained  
473 enabled us to quantify the emissions from that fire and evaluate the possible impact on air quality  
474 in suburban Orléans.

475 Average concentrations of  $PM_{2.5}$  and  $PM_{10}$  in September were  $6.7$  and  $12.8 \mu g m^{-3}$ , respectively,  
476 which are close to or lower than the updated WHO air quality guideline values of  $5$  and  $15 \mu g m^{-3}$ ,  
477 respectively. However,  $PM_{2.5}$  and  $PM_{10}$  levels in the periods that were affected by wildfire  
478 emissions increased substantially ( $29.6$  and  $42.6 \mu g m^{-3}$ , respectively) and exceeded the WHO air  
479 quality guideline values (Figure 3). Additionally, levels of a series of VOCs including BTEX  
480 were also enhanced by the wildfire event.

481 Besides, the impacts of the wildfire on the size, composition, and properties of aerosol were  
482 quantified. Within the wildfire plume, an increase in BC was observed and the observed  
483  $BC_{wb}/BC_{ff}$  ratio of  $0.32$  was in the range of values ( $0.3 - 0.5$ ) impacted by wildfire emissions.  
484 Aerosol pH was significantly reduced in the plume as a result of the increase in sulfate. Besides,  
485 Emission factors compared to CO were calculated for various gaseous pollutants and compared  
486 with previous studies. Relatively higher EF ratios for GHGs ( $CH_4$  and  $N_2O$ ) were found within  
487 the plume from this wildfire, indicative of the possibly important role of small fires in GHGs  
488 burden.

489 Furthermore, emissions of this wildfire were estimated and compared with GFAS emission  
490 inventory. We found that the GFAS emission inventory significantly underestimated the  
491 emission from this small fire, which agrees with other studies (Ramo et al., 2021; Wang et al.,  
492 2021). This study suggested that the detection and prediction of small fire emissions still need  
493 further assessment and improvement.

494 The year 2020 was a warm year in Europe, with the autumn having the highest recorded  
495 temperatures since 1950 (see ECWMF news at  
496 <https://climate.copernicus.eu/esotc/2020/temperature>, last access: 17 January 2022). Higher  
497 temperatures are expected to lead to wildfire events in wildfire hotspot regions as well as those  
498 regions where few wildfires were recorded before (e.g., Orléans) (Liu et al., 2010; Randerson et  
499 al., 2012), which may be exacerbated by climate change. This not only reduces regional air  
500 quality near those wildfires but also increases global greenhouse gas emissions. We suggest that  
501 besides the major wildfire regions, attention should also be paid to the regions with few wildfires  
502 recorded so far, in order to better understand their environmental effects and how their  
503 distribution may change over time.

## 504 Acknowledgments

505 We thank Ministère de l’Agriculture et de l’Alimentation for providing information (including  
506 the photo) about the wildfire.

## 507 Author Contribution

508 A.M. and V.C. led this study. C.X., B.G., Y.R., M.C., P.M., F.L.F., and C.R. performed the  
509 measurements. C.X. and G.K. performed the model simulations. C.X. took the lead in data  
510 analysis and manuscript writing with input from all co-authors. V.D., Y.M., MMG, A.M., and  
511 V.C. revised the manuscript. All authors discussed the results and approved the final manuscript.

## 512 Funding

513 This study was supported by the VOLTAIRE project (ANR-10-LABX-100-01) funded by the  
514 ANR and the PIVOTS project provided by the Region Centre – Val de Loire (ARD 2020  
515 program and CPER 2015 – 2020).

## 516 Competing Interests

517 The authors declare no competing financial interest.

## 518 Data Availability

519 All the data presented in this study are available upon request from the corresponding authors.

## 520 References

- 521 Akagi, S.K., Yokelson, R.J., Wiedinmyer, C., Alvarado, M.J., Reid, J.S., Karl, T., Crouse, J.D., Wennberg, P.O.,  
522 2011. Emission factors for open and domestic biomass burning for use in atmospheric models. *Atmos. Chem.*  
523 *Phys.* 11, 4039–4072. <https://doi.org/10.5194/acp-11-4039-2011>
- 524 Andreae, M.O., 2019. Emission of trace gases and aerosols from biomass burning - An updated assessment. *Atmos.*  
525 *Chem. Phys.* 19, 8523–8546. <https://doi.org/10.5194/acp-19-8523-2019>
- 526 Andreae, M.O., Merlet, P., 2001. Emission of trace gases and aerosols from biomass burning. *Global Biogeochem.*  
527 *Cycles* 15, 955–966. <https://doi.org/10.1029/2000GB001382>
- 528 Artés, T., Oom, D., de Rigo, D., Durrant, T.H., Maianti, P., Libertà, G., San-Miguel-Ayanz, J., 2019. A global  
529 wildfire dataset for the analysis of fire regimes and fire behaviour. *Sci. Data* 6, 296.  
530 <https://doi.org/10.1038/s41597-019-0312-2>
- 531 Atkinson, R., Arey, J., 2003. Atmospheric Degradation of Volatile Organic Compounds. *Chem. Rev.* 103, 4605–  
532 4638. <https://doi.org/10.1021/cr0206420>
- 533 Baray, J.L., Dufлот, V., Posny, F., Cammas, J.P., Thompson, A.M., Gabarrot, F., Bonne, J.L., Zeng, G., 2012. One  
534 year ozonesonde measurements at Kerguelen Island (49.2°S, 70.1°E): Influence of stratosphere-to-troposphere  
535 exchange and long-range transport of biomass burning plumes. *J. Geophys. Res. Atmos.* 117, 1–10.  
536 <https://doi.org/10.1029/2011JD016717>
- 537 Barbero, R., Abatzoglou, J.T., Larkin, N.K., Kolden, C.A., Stocks, B., 2015. Climate change presents increased  
538 potential for very large fires in the contiguous United States. *Int. J. Wildl. Fire* 24, 892–899.  
539 <https://doi.org/10.1071/WF15083>
- 540 Brocchi, V., Krysztofiak, G., Catoire, V., Guth, J., Marécal, V., Zbinden, R., El Amraoui, L., Dulac, F., Ricaud, P.,  
541 2018. Intercontinental transport of biomass burning pollutants over the Mediterranean Basin during the  
542 summer 2014 ChArMEx-GLAM airborne campaign. *Atmos. Chem. Phys.* 18, 6887–6906.  
543 <https://doi.org/10.5194/acp-18-6887-2018>
- 544 Brocchi, V., Krysztofiak, G., Deroubaix, A., Stratmann, G., Sauer, D., Schlager, H., Deetz, K., Dayma, G., Robert,  
545 C., Chevrier, S., Catoire, V., 2019. Local air pollution from oil rig emissions observed during the airborne  
546 DACCIWA campaign. *Atmos. Chem. Phys.* 19, 11401–11411. <https://doi.org/10.5194/acp-19-11401-2019>
- 547 Burling, I.R., Yokelson, R.J., Griffith, D.W.T., Johnson, T.J., Veres, P., Roberts, J.M., Warneke, C., Urbanski, S.P.,  
548 Reardon, J., Weise, D.R., Hao, W.M., De Gouw, J., 2010. Laboratory measurements of trace gas emissions  
549 from biomass burning of fuel types from the southeastern and southwestern United States. *Atmos. Chem.*  
550 *Phys.* 10, 11115–11130. <https://doi.org/10.5194/acp-10-11115-2010>
- 551 Cai, M., Ren, Y., Gibilisco, R.G., Grosselin, B., McGillen, M.R., Xue, C., Mellouki, A., Daële, V., 2022. Ambient  
552 BTEX concentrations during the COVID-19 lockdown in a peri-urban environment (Orléans, France).  
553 *Atmosphere (Basel)*. 13. <https://doi.org/10.3390/atmos13010010>
- 554 Catoire, V., Robert, C., Chartier, M., Jacquet, P., Guimbaud, C., Krysztofiak, G., 2017. The SPIRIT airborne  
555 instrument: a three-channel infrared absorption spectrometer with quantum cascade lasers for in situ



556 atmospheric trace-gas measurements. *Appl. Phys. B* 123, 244. <https://doi.org/10.1007/s00340-017-6820-x>

557 Chaliyakunnel, S., Millet, D.B., Wells, K.C., Cady-Pereira, K.E., Shephard, M.W., 2016. A Large Underestimate of  
558 Formic Acid from Tropical Fires: Constraints from Space-Borne Measurements. *Environ. Sci. Technol.* 50,  
559 5631–5640. <https://doi.org/10.1021/acs.est.5b06385>

560 Collier, S., Zhou, S., Onasch, T.B., Jaffe, D.A., Kleinman, L., Sedlacek, A.J., Briggs, N.L., Hee, J., Fortner, E.,  
561 Shilling, J.E., Worsnop, D., Yokelson, R.J., Parworth, C., Ge, X., Xu, J., Butterfield, Z., Chand, D., Dubey,  
562 M.K., Pekour, M.S., Springston, S., Zhang, Q., 2016. Regional Influence of Aerosol Emissions from Wildfires  
563 Driven by Combustion Efficiency: Insights from the BBOP Campaign. *Environ. Sci. Technol.* 50, 8613–8622.  
564 <https://doi.org/10.1021/acs.est.6b01617>

565 David, L.M., Ravishankara, A.R., Brey, S.J., Fischer, E. V, Volckens, J., Kreidenweis, S., 2021. Could the exception  
566 become the rule? “Uncontrollable” air pollution events in the U.S. due to wildland fires. *Environ. Res. Lett.*  
567 16, 034029. <https://doi.org/10.1088/1748-9326/abe1f3>

568 Di Giuseppe, F., Rémy, S., Pappenberger, F., Wetterhall, F., 2018. Using the Fire Weather Index (FWI) to improve  
569 the estimation of fire emissions from fire radiative power (FRP) observations. *Atmos. Chem. Phys.* 18, 5359–  
570 5370. <https://doi.org/10.5194/acp-18-5359-2018>

571 Fountoukis, C., Nenes, A., 2007. ISORROPIA II: a computationally efficient thermodynamic equilibrium model for  
572  $K^+$ - $Ca^{2+}$ - $Mg^{2+}$ - $NH_4^+$ - $Na^+$ - $SO_4^{2-}$ - $NO_3^-$ - $Cl^-$ - $H_2O$  aerosols. *Atmos. Chem. Phys.* 7, 4639–4659.  
573 <https://doi.org/10.5194/acp-7-4639-2007>

574 French, N.H.F., Kasischke, E.S., Williams, D.G., 2002. Variability in the emission of carbon-based trace gases from  
575 wildfire in the Alaskan boreal forest. *J. Geophys. Res.* 108, 8151. <https://doi.org/10.1029/2001JD000480>

576 Friedlingstein, P., O’Sullivan, M., Jones, M.W., Andrew, R.M., Hauck, J., Olsen, A., Peters, G.P., Peters, W.,  
577 Pongratz, J., Sitch, S., Le Quéré, C., Canadell, J.G., Ciais, P., Jackson, R.B., Alin, S., Aragão, L.E.O.C.,  
578 Arneeth, A., Arora, V., Bates, N.R., Becker, M., Benoit-Cattin, A., Bittig, H.C., Bopp, L., Bultan, S., Chandra,  
579 N., Chevallier, F., Chini, L.P., Evans, W., Florentie, L., Forster, P.M., Gasser, T., Gehlen, M., Gilfillan, D.,  
580 Gkritzalis, T., Gregor, L., Gruber, N., Harris, I., Hartung, K., Haverd, V., Houghton, R.A., Ilyina, T., Jain,  
581 A.K., Joetzjer, E., Kadono, K., Kato, E., Kitidis, V., Korsbakken, J.I., Landschützer, P., Lefèvre, N., Lenton,  
582 A., Lienert, S., Liu, Z., Lombardozzi, D., Marland, G., Metzl, N., Munro, D.R., Nabel, J.E.M.S., Nakaoka,  
583 S.I., Niwa, Y., O’Brien, K., Ono, T., Palmer, P.I., Pierrot, D., Poulter, B., Resplandy, L., Robertson, E.,  
584 Rödenbeck, C., Schwinger, J., Séférian, R., Skjelvan, I., Smith, A.J.P., Sutton, A.J., Tanhua, T., Tans, P.P.,  
585 Tian, H., Tilbrook, B., Van Der Werf, G., Vuichard, N., Walker, A.P., Wanninkhof, R., Watson, A.J., Willis,  
586 D., Wiltshire, A.J., Yuan, W., Yue, X., Zaehle, S., 2020. Global Carbon Budget 2020. *Earth Syst. Sci. Data*  
587 12, 3269–3340. <https://doi.org/10.5194/essd-12-3269-2020>

588 Gallagher, M.W., Nemitz, E., Dorsey, J.R., Fowler, D., Sutton, M.A., Flynn, M., Duyzer, J., 2002. Measurements  
589 and parameterizations of small aerosol deposition velocities to grassland, arable crops, and forest: Influence of  
590 surface roughness length on deposition. *J. Geophys. Res. Atmos.* 107, 4154.  
591 <https://doi.org/10.1029/2001JD000817>

592 Granier, C., Müller, J.-F., Brasseur, G., 2000. The Impact of Biomass Burning on the Global Budget of Ozone and

593 Ozone Precursors. Springer, Dordrecht, pp. 69–85. [https://doi.org/10.1007/0-306-47959-1\\_5](https://doi.org/10.1007/0-306-47959-1_5)

594 Helin, A., Niemi, J. V., Virkkula, A., Pirjola, L., Teinilä, K., Backman, J., Aurela, M., Saarikoski, S., Rönkkö, T.,  
595 Asmi, E., Timonen, H., 2018. Characteristics and source apportionment of black carbon in the Helsinki  
596 metropolitan area, Finland. *Atmos. Environ.* 190, 87–98. <https://doi.org/10.1016/j.atmosenv.2018.07.022>

597 Herich, H., Hueglin, C., Buchmann, B., 2011. A 2.5 year’s source apportionment study of black carbon from wood  
598 burning and fossil fuel combustion at urban and rural sites in Switzerland. *Atmos. Meas. Tech.* 4, 1409–1420.  
599 <https://doi.org/10.5194/amt-4-1409-2011>

600 Hersbach, H., Bell, B., Berrisford, P., Hirahara, S., Horányi, A., Muñoz- Sabater, J., Nicolas, J., Peubey, C., Radu,  
601 R., Schepers, D., Simmons, A., Soci, C., Abdalla, S., Abellan, X., Balsamo, G., Bechtold, P., Biavati, G.,  
602 Bidlot, J., Bonavita, M., Chiara, G., Dahlgren, P., Dee, D., Diamantakis, M., Dragani, R., Flemming, J.,  
603 Forbes, R., Fuentes, M., Geer, A., Haimberger, L., Healy, S., Hogan, R.J., Hólm, E., Janisková, M., Keeley,  
604 S., Laloyaux, P., Lopez, P., Lupu, C., Radnoti, G., Rosnay, P., Rozum, I., Vamborg, F., Villaume, S., Thépaut,  
605 J., 2020. The ERA5 global reanalysis. *Q. J. R. Meteorol. Soc.* 146, 1999–2049. <https://doi.org/10.1002/qj.3803>

606 Hirsch, E., Koren, I., 2021. Record-breaking aerosol levels explained by smoke injection into the stratosphere.  
607 *Science* 371, 1269–1274. <https://doi.org/10.1126/science.abe1415>

608 Hodshire, A.L., Akherati, A., Alvarado, M.J., Brown-Steiner, B., Jathar, S.H., Jimenez, J.L., Kreidenweis, S.M.,  
609 Lonsdale, C.R., Onasch, T.B., Ortega, A.M., Pierce, J.R., 2019. Aging Effects on Biomass Burning Aerosol  
610 Mass and Composition: A Critical Review of Field and Laboratory Studies. *Environ. Sci. Technol.* 53, 10007–  
611 10022. <https://doi.org/10.1021/acs.est.9b02588>

612 Hooghiem, J.J.D., Popa, M.E., Röckmann, T., Grooß, J.-U., Tritscher, I., Müller, R., Kivi, R., Chen, H., 2020.  
613 Wildfire smoke in the lower stratosphere identified by in situ CO observations. *Atmos. Chem. Phys.* 20,  
614 13985–14003. <https://doi.org/10.5194/acp-20-13985-2020>

615 Jaffe, D.A., Wigder, N.L., 2012. Ozone production from wildfires: A critical review. *Atmos. Environ.* 51, 1–10.  
616 <https://doi.org/10.1016/j.atmosenv.2011.11.063>

617 Jiang, Z., Gosselin, B., Daële, V., Mellouki, A., Mu, Y., 2017. Seasonal and diurnal variations of BTEX  
618 compounds in the semi-urban environment of Orleans, France. *Sci. Total Environ.* 574, 1659–1664.  
619 <https://doi.org/10.1016/j.scitotenv.2016.08.214>

620 Jost, C., Trentmann, J., Sprung, D., Andreae, M.O., McQuaid, J.B., Barjat, H., 2003. Trace gas chemistry in a young  
621 biomass burning plume over Namibia: Observations and model simulations. *J. Geophys. Res. Atmos.* 108.  
622 <https://doi.org/10.1029/2002JD002431>

623 Kalogridis, A.C., Vratolis, S., Liakakou, E., Gerasopoulos, E., Mihalopoulos, N., Eleftheriadis, K., 2018.  
624 Assessment of wood burning versus fossil fuel contribution to wintertime black carbon and carbon monoxide  
625 concentrations in Athens, Greece. *Atmos. Chem. Phys.* 18, 10219–10236. <https://doi.org/10.5194/acp-18-10219-2018>

626

627 Kloss, C., Berthet, G., Sellitto, P., Ploeger, F., Bucci, S., Khaykin, S., Jégou, F., Taha, G., Thomason, L.W., Barret,  
628 B., Le Flochmoen, E., Von Hobe, M., Bossolasco, A., Bègue, N., Legras, B., 2019. Transport of the 2017  
629 canadian wildfire plume to the tropics via the asian monsoon circulation. *Atmos. Chem. Phys.* 19, 13547–

630 13567. <https://doi.org/10.5194/acp-19-13547-2019>

631 Kloss, C., Sellitto, P., von Hobe, M., Berthet, G., Smale, D., Krysztofiak, G., Xue, C., Qiu, C., Jégou, F.,  
632 Ouerghemmi, I., Legras, B., 2021. Australian Fires 2019–2020: Tropospheric and Stratospheric Pollution  
633 Throughout the Whole Fire Season. *Front. Environ. Sci.* 9, 1–11. <https://doi.org/10.3389/fenvs.2021.652024>

634 Krysztofiak, G., Catoire, V., Hamer, P.D., Marécal, V., Robert, C., Engel, A., Bönisch, H., Grossmann, K., Quack,  
635 B., Atlas, E., Pfeilsticker, K., 2018. Evidence of convective transport in tropical West Pacific region during  
636 SHIVA experiment. *Atmos. Sci. Lett.* 19, 1–7. <https://doi.org/10.1002/asl.798>

637 Li, S., Liu, D., Hu, D., Kong, S., Wu, Y., Ding, S., Cheng, Y., Qiu, H., Zheng, S., Yan, Q., Zheng, H., Hu, K.,  
638 Zhang, J., Zhao, D., Liu, Q., Sheng, J., Ye, J., He, H., Ding, D., 2021. Evolution of Organic Aerosol From  
639 Wood Smoke Influenced by Burning Phase and Solar Radiation. *J. Geophys. Res. Atmos.* 126, 1–16.  
640 <https://doi.org/10.1029/2021JD034534>

641 Liu, Y., Stanturf, J., Goodrick, S., 2010. Trends in global wildfire potential in a changing climate. *For. Ecol.*  
642 *Manage.* 259, 685–697. <https://doi.org/10.1016/j.foreco.2009.09.002>

643 Mellouki, A., Ammann, M., Cox, R.A., Crowley, J.N., Herrmann, H., Jenkin, M.E., McNeill, V.F., Troe, J.,  
644 Wallington, T.J., 2021. Evaluated kinetic and photochemical data for atmospheric chemistry: volume VIII –  
645 gas-phase reactions of organic species with four, or more, carbon atoms ( $\geq$   
646 C&lt;sub&gt;4&lt;/sub&gt;). *Atmos. Chem. Phys.* 21, 4797–4808.  
647 <https://doi.org/10.5194/acp-21-4797-2021>

648 Nie, W., Ding, A.J., Xie, Y.N., Xu, Z., Mao, H., Kerminen, V.-M., Zheng, L.F., Qi, X.M., Huang, X., Yang, X.-Q.,  
649 Sun, J.N., Herrmann, E., Petäjä, T., Kulmala, M., Fu, C.B., 2015. Influence of biomass burning plumes on  
650 HONO chemistry in eastern China. *Atmos. Chem. Phys.* 15, 1147–1159. [https://doi.org/10.5194/acp-15-1147-](https://doi.org/10.5194/acp-15-1147-2015)  
651 2015

652 Peng, Q., Palm, B.B., Melander, K.E., Lee, B.H., Hall, S.R., Ullmann, K., Campos, T., Weinheimer, A.J., Apel,  
653 E.C., Hornbrook, R.S., Hills, A.J., Montzka, D.D., Flocke, F., Hu, L., Permar, W., Wielgasz, C., Lindaas, J.,  
654 Pollack, I.B., Fischer, E. V., Bertram, T.H., Thornton, J.A., 2020. HONO Emissions from Western U.S.  
655 Wildfires Provide Dominant Radical Source in Fresh Wildfire Smoke. *Environ. Sci. Technol.* 54, 5954–5963.  
656 <https://doi.org/10.1021/acs.est.0c00126>

657 Pisso, I., Sollum, E., Grythe, H., Kristiansen, N.I., Cassiani, M., Eckhardt, S., Arnold, D., Morton, D., Thompson,  
658 R.L., Groot Zwaftink, C.D., Evangeliou, N., Sodemann, H., Haimberger, L., Henne, S., Brunner, D.,  
659 Burkhardt, J.F., Fouilloux, A., Brioude, J., Philipp, A., Seibert, P., Stohl, A., 2019. The Lagrangian particle  
660 dispersion model FLEXPART version 10.4. *Geosci. Model Dev.* 12, 4955–4997. [https://doi.org/10.5194/gmd-](https://doi.org/10.5194/gmd-12-4955-2019)  
661 12-4955-2019

662 Quegan, S., Le Toan, T., Chave, J., Dall, J., Exbrayat, J.F., Minh, D.H.T., Lomas, M., D’Alessandro, M.M., Paillou,  
663 P., Papathanassiou, K., Rocca, F., Saatchi, S., Scipal, K., Shugart, H., Smallman, T.L., Soja, M.J., Tebaldini,  
664 S., Ulander, L., Villard, L., Williams, M., 2019. The European Space Agency BIOMASS mission: Measuring  
665 forest above-ground biomass from space. *Remote Sens. Environ.* <https://doi.org/10.1016/j.rse.2019.03.032>

666 R’Honi, Y., Clarisse, L., Clerbaux, C., Hurtmans, D., Dufлот, V., Turquety, S., Ngadi, Y., Coheur, P.F., 2013.

667 Exceptional emissions of NH<sub>3</sub> and HCOOH in the 2010 Russian wildfires. *Atmos. Chem. Phys.* 13, 4171–  
668 4181. <https://doi.org/10.5194/acp-13-4171-2013>

669 Ramo, R., Roteta, E., Bistinas, I., van Wees, D., Bastarrika, A., Chuvieco, E., van der Werf, G.R., 2021. African  
670 burned area and fire carbon emissions are strongly impacted by small fires undetected by coarse resolution  
671 satellite data. *Proc. Natl. Acad. Sci.* 118, e2011160118. <https://doi.org/10.1073/pnas.2011160118>

672 Randerson, J.T., Chen, Y., van der Werf, G.R., Rogers, B.M., Morton, D.C., 2012. Global burned area and biomass  
673 burning emissions from small fires. *J. Geophys. Res. Biogeosciences* 117, G4012.  
674 <https://doi.org/10.1029/2012JG002128>

675 Saunois, M., Stavert, A.R., Poulter, B., Bousquet, P., Canadell, J.G., Jackson, R.B., Raymond, P.A., Dlugokencky,  
676 E.J., Houweling, S., Patra, P.K., Ciais, P., Arora, V.K., Bastviken, D., Bergamaschi, P., Blake, D.R.,  
677 Brailsford, G., Bruhwiler, L., Carlson, K.M., Carrol, M., Castaldi, S., Chandra, N., Crevoisier, C., Crill, P.M.,  
678 Covey, K., Curry, C.L., Etiope, G., Frankenberg, C., Gedney, N., Hegglin, M.I., Höglund-Isaksson, L.,  
679 Hugelius, G., Ishizawa, M., Ito, A., Janssens-Maenhout, G., Jensen, K.M., Joos, F., Kleinen, T., Krummel,  
680 P.B., Langenfelds, R.L., Laruelle, G.G., Liu, L., Machida, T., Maksyutov, S., McDonald, K.C., McNorton, J.,  
681 Miller, P.A., Melton, J.R., Morino, I., Müller, J., Murguía-Flores, F., Naik, V., Niwa, Y., Noce, S., O'Doherty,  
682 S., Parker, R.J., Peng, C., Peng, S., Peters, G.P., Prigent, C., Prinn, R., Ramonet, M., Regnier, P., Riley, W.J.,  
683 Rosentreter, J.A., Segers, A., Simpson, I.J., Shi, H., Smith, S.J., Steele, L.P., Thornton, B.F., Tian, H.,  
684 Tohjima, Y., Tubiello, F.N., Tsuruta, A., Viovy, N., Voulgarakis, A., Weber, T.S., van Weele, M., van der  
685 Werf, G.R., Weiss, R.F., Worthy, D., Wunch, D., Yin, Y., Yoshida, Y., Zhang, W., Zhang, Z., Zhao, Y.,  
686 Zheng, B., Zhu, Qing, Zhu, Qian, Zhuang, Q., 2020. The Global Methane Budget 2000–2017. *Earth Syst.*  
687 *Sci. Data* 12, 1561–1623. <https://doi.org/10.5194/essd-12-1561-2020>

688 Seiler, W., Crutzen, P.J., 1980. Estimates of gross and net fluxes of carbon between the biosphere and the  
689 atmosphere from biomass burning. *Clim. Change.* <https://doi.org/10.1007/BF00137988>

690 Seinfeld, J.H., Pandis, S.N., 2016. *Atmospheric Chemistry and Physics: From Air Pollution to Climate Change*,  
691 John Wiley & Sons. John Wiley & Sons.

692 Tang, Y.S., Flechard, C.R., Dämmgen, U., Vidic, S., Djuricic, V., Mitosinkova, M., Uggerud, H.T., Sanz, M.J.,  
693 Simmons, I., Dragosits, U., Nemitz, E., Twigg, M., van Dijk, N., Fauvel, Y., Sanz, F., Ferm, M., Perrino, C.,  
694 Catrambone, M., Leaver, D., Braban, C.F., Cape, J.N., Heal, M.R., Sutton, M.A., 2021. Pan-European rural  
695 monitoring network shows dominance of NH<sub>3</sub> gas and NH<sub>4</sub>NO<sub>3</sub> aerosol in inorganic atmospheric pollution  
696 load. *Atmos. Chem. Phys.* 21, 875–914. <https://doi.org/10.5194/acp-21-875-2021>

697 Theys, N., Volkamer, R., Müller, J.-F., Zarzana, K.J., Kille, N., Clarisse, L., De Smedt, I., Lerot, C., Finkenzeller,  
698 H., Hendrick, F., Koenig, T.K., Lee, C.F., Knote, C., Yu, H., Van Roozendaal, M., 2020. Global nitrous acid  
699 emissions and levels of regional oxidants enhanced by wildfires. *Nat. Geosci.* 13, 681–686.  
700 <https://doi.org/10.1038/s41561-020-0637-7>

701 Van Der Werf, G.R., Randerson, J.T., Giglio, L., Van Leeuwen, T.T., Chen, Y., Rogers, B.M., Mu, M., Van Marle,  
702 M.J.E., Morton, D.C., Collatz, G.J., Yokelson, R.J., Kasibhatla, P.S., 2017. Global fire emissions estimates  
703 during 1997-2016. *Earth Syst. Sci. Data* 9, 697–720. <https://doi.org/10.5194/essd-9-697-2017>

704 Wang, S., Coggon, M.M., Gkatzelis, G.I., Warneke, C., Bourgeois, I., Ryerson, T., Peischl, J., Veres, P.R., Neuman,  
705 J.A., Hair, J., Shingler, T., Fenn, M., Diskin, G., Huey, L.G., Lee, Y.R., Apel, E.C., Hornbrook, R.S., Hills,  
706 A.J., Hall, S.R., Ullmann, K., Bela, M.M., Trainer, M.K., Kumar, R., Orlando, J.J., Flocke, F.M., Emmons,  
707 L.K., 2021. Chemical Tomography in a Fresh Wildland Fire Plume: A Large Eddy Simulation (LES) Study. *J.*  
708 *Geophys. Res. Atmos.* 126. <https://doi.org/10.1029/2021JD035203>

709 Wiedinmyer, C., Akagi, S.K., Yokelson, R.J., Emmons, L.K., Al-Saadi, J.A., Orlando, J.J., Soja, A.J., 2011. The  
710 Fire INventory from NCAR (FINN): A high resolution global model to estimate the emissions from open  
711 burning. *Geosci. Model Dev.* 4, 625–641. <https://doi.org/10.5194/gmd-4-625-2011>

712 Xu, L., Crouse, J.D., Vasquez, K.T., Allen, H., Wennberg, P.O., Bourgeois, I., Brown, S.S., Campuzano-Jost, P.,  
713 Coggon, M.M., Crawford, J.H., DiGangi, J.P., Diskin, G.S., Fried, A., Gargulinski, E.M., Gilman, J.B.,  
714 Gkatzelis, G.I., Guo, H., Hair, J.W., Hall, S.R., Halliday, H.A., Hanisco, T.F., Hannun, R.A., Holmes, C.D.,  
715 Huey, L.G., Jimenez, J.L., Lamplugh, A., Lee, Y.R., Liao, J., Lindaas, J., Neuman, J.A., Nowak, J.B., Peischl,  
716 J., Peterson, D.A., Piel, F., Richter, D., Rickly, P.S., Robinson, M.A., Rollins, A.W., Ryerson, T.B., Sekimoto,  
717 K., Selimovic, V., Shingler, T., Soja, A.J., St. Clair, J.M., Tanner, D.J., Ullmann, K., Veres, P.R., Walega, J.,  
718 Warneke, C., Washenfelder, R.A., Weibring, P., Wisthaler, A., Wolfe, G.M., Womack, C.C., Yokelson, R.J.,  
719 2021. Ozone chemistry in western U.S. wildfire plumes. *Sci. Adv.* 7. <https://doi.org/10.1126/sciadv.abl3648>

720 Yttri, K.E., Lund Myhre, C., Eckhardt, S., Fiebig, M., Dye, C., Hirdman, D., Ström, J., Klimont, Z., Stohl, A., 2014.  
721 Quantifying black carbon from biomass burning by means of levoglucosan - A one-year time series at the  
722 Arctic observatory Zeppelin. *Atmos. Chem. Phys.* 14, 6427–6442. <https://doi.org/10.5194/acp-14-6427-2014>

723 Yu, P., Toon, O.B., Bardeen, C.G., Zhu, Y., Rosenlof, K.H., Portmann, R.W., Thornberry, T.D., Gao, R.-S., Davis,  
724 S.M., Wolf, E.T., de Gouw, J., Peterson, D.A., Fromm, M.D., Robock, A., 2019. Black carbon lofts wildfire  
725 smoke high into the stratosphere to form a persistent plume. *Science* 365, 587–590.  
726 <https://doi.org/10.1126/science.aax1748>

727 Zheng, B., Chevallier, F., Yin, Y., Ciais, P., Fortems-Cheiney, A., Deeter, M.N., Parker, R.J., Wang, Y., Worden,  
728 H.M., Zhao, Y., 2019. Global atmospheric carbon monoxide budget 2000–2017 inferred from multi-species  
729 atmospheric inversions. *Earth Syst. Sci. Data* 11, 1411–1436. <https://doi.org/10.5194/essd-11-1411-2019>

730